
Height-Guided Projection Reparameterization for Camera-LiDAR Occupancy

Yuan Wu¹ Zhiqiang Yan² Jiawei Lian¹ Zhengxue Wang¹ Jian Yang¹

¹Nanjing University of Science and Technology

²National University of Singapore

Abstract

3D occupancy prediction aims to infer dense, voxel-wise scene semantics from sensor observations, where the 2D-to-3D view transformation serves as a crucial step in bridging image features and volumetric representations. Most previous methods rely on a fixed projection space, where 3D reference points are uniformly sampled along pillars. However, such sampling struggles to capture the sparsity and height variations of real-world scenes, leading to ambiguous correspondences and unreliable feature aggregation. To address these challenges, we propose **HiPR**, a camera-LiDAR occupancy framework with **Height-Guided Projection Reparameterization**. HiPR first encodes LiDAR into a BEV height map to capture the maximum height of the point cloud. HiPR then adjusts the sampling range of each pillar using the height prior, enabling adaptive reparameterization of the projection space. As a result, the projected points are redistributed into geometrically meaningful regions rather than fixed ranges. Meanwhile, we mask out the invalid parts of the height map to avoid misleading the feature aggregation. In addition, to alleviate the training instability caused by noisy LiDAR-derived heights, we introduce a training-time Progressive Height Conditioning strategy, which gradually transitions the conditioning signal from ground-truth heights to LiDAR heights. Extensive experiments demonstrate that HiPR consistently outperforms existing state-of-the-art methods while maintaining real-time inference. The code and pretrained models can be found at <https://github.com/Rayn-Wu/HiPR>.

1 Introduction

3D occupancy prediction [31, 45, 46, 51, 59] aims to estimate voxel-wise scene semantics from sensor observations and is crucial for holistic scene understanding and motion planning in autonomous driving [9, 10, 28, 52, 57]. Camera-based occupancy prediction [2, 4, 5, 20, 25] has attracted increasing attention, as cameras provide rich semantic cues at low cost and with wide coverage. To further improve performance, recent works [33, 47, 48, 53, 56] increasingly explore multi-modal frameworks that integrate complementary signals from LiDAR or radar.

Despite these advances, accurately lifting 2D image features into 3D space remains a critical challenge. In most previous methods, image features are associated with BEV queries through backward projection [23, 24, 26], where a set of 3D reference points is projected onto image planes for feature aggregation. However, these points are predefined and uniformly sampled along globally shared pillars. Such a fixed projection space struggles to capture the sparsity and height variations of real-world scenes. As illustrated in Fig. 1(a), a car and a tall tree occupy vastly different height ranges. When using a fixed projection space (Fig. 1(b)), 3D reference points sampled above the car inevitably misalign with the actual object, leading to the erroneous aggregation of background features (e.g., the sky) instead of the target semantics. Furthermore, even for entirely empty regions devoid of objects, this fixed paradigm still redundantly assigns dense 3D reference points, forcing

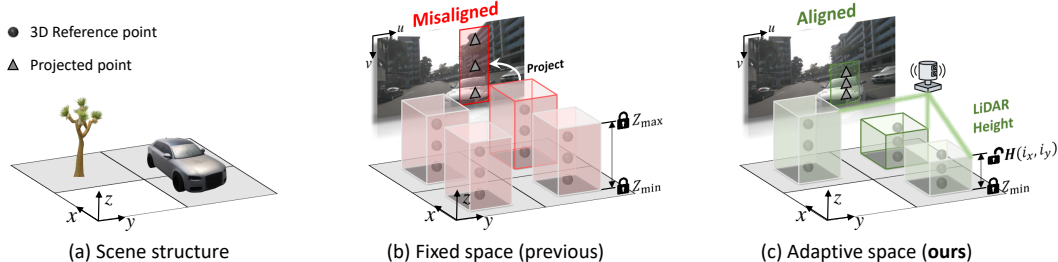


Figure 1: (a) Scene structure with varying heights. (b) Previous methods rely on a predefined fixed projection space, causing semantic misalignment on the 2D image plane. (c) Our method utilizes the LiDAR height prior to adaptively bound the sampling space of each pillar, ensuring alignment between projected reference points and scene structures for reliable feature aggregation.

the network to aggregate meaningless image features. Consequently, this fixed projection space introduces ambiguous correspondences and unreliable feature aggregation.

To address these challenges, we propose HiPR, a camera-LiDAR occupancy framework with Height-Guided Projection Reparameterization. Specifically, as shown in Fig. 1(c), we first encode the LiDAR point cloud into a BEV height map, which captures the maximum height of the point cloud. Based on this height prior, we adjust the sampling range of each pillar. As a result, the 3D reference points are redistributed into geometrically meaningful regions rather than fixed height ranges. This enables the projected points to better align with the underlying scene structures in the image space, leading to more consistent and reliable feature aggregation. In addition, for BEV locations without LiDAR heights, we directly mask out the corresponding regions to prevent unreliable feature aggregation.

Moreover, to alleviate the training instability caused by noisy LiDAR-derived heights, we propose a training-time Progressive Height Conditioning strategy, which gradually transitions the conditioning signal from dense ground-truth heights to LiDAR heights during training.

Our main contributions are summarized as follows:

- We introduce a novel camera-LiDAR occupancy paradigm, which, for the first time, leverages the LiDAR height prior to guide the 2D-to-3D view transformation process.
- We propose HiPR, which (i) reparameterizes the projection space using a LiDAR-derived height map to align with the scene structure, and (ii) introduces a training-only Progressive Height Conditioning strategy to mitigate the impact of noisy LiDAR heights.
- Extensive experiments demonstrate that HiPR achieves state-of-the-art performance. Moreover, a lightweight variant outperforms existing real-time approaches, yielding a favorable trade-off between accuracy and efficiency. Code and weights are released for peer research.

2 Related Work

Multi-modal 3D Occupancy Prediction. Multi-modal 3D occupancy perception [11, 32, 43, 45, 47, 48, 53, 56] leverages complementary information from multiple sensors to overcome the inherent limitations of single-modality perception. A common paradigm is to first lift image features into 3D space and then fuse them with point cloud features. For instance, OccFusion [33] concatenates 3D features from different modalities along the feature dimension, followed by multi-scale feature extraction. However, the sensor sparsity and modality-specific visibility limit the effectiveness of naive feature concatenation. To address this issue, Co-Occ [35] enhances LiDAR features using neighboring camera features, and further introduces an implicit volumetric rendering-based regularization to supervise the fused features. In contrast, DAOcc [53] introduces 3D object detection as an auxiliary training task, providing additional supervision and improving performance on foreground categories. Beyond fusion strategies based on simple feature concatenation, recent works [41, 47, 56] have explored more adaptive fusion mechanisms. For example, REOcc [41] employs cross-attention to fuse camera and radar BEV features. While effective, attention-based fusion introduces considerable computational overhead. To improve efficiency, Occ-Mamba [38] uses feature reordering to achieve global modeling with linear complexity. In addition to BEV-level fusion, incorporating 2D perspective-

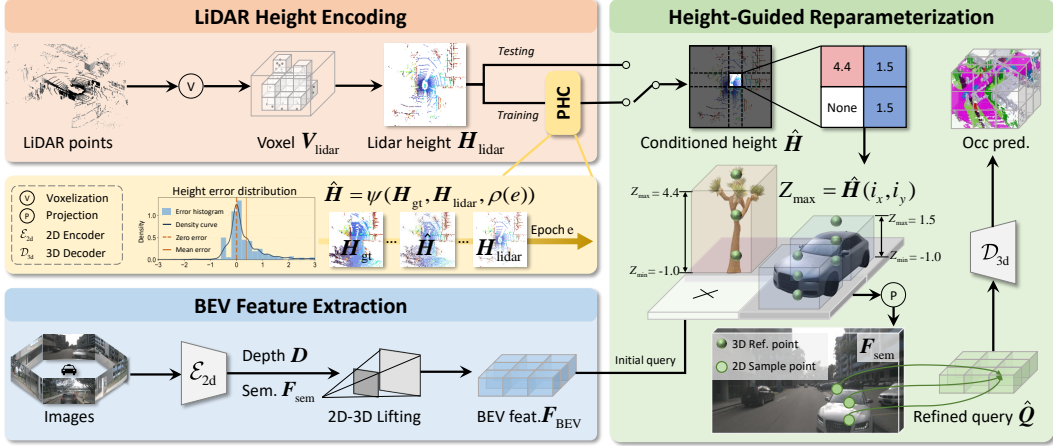


Figure 2: Overview of HiPR. Multi-view images are first transformed into a coarse BEV feature serving as the initial BEV query. Meanwhile, the LiDAR point cloud is encoded into a BEV height map and conditioned by PHC during training. Guided by the height map, the initial BEV query is refined through Height-Guided Reparameterization and finally decoded for 3D occupancy prediction.

view (PV) features has been shown to further refine 3D representations. For example, HyDRa [48] enhances PV features using BEV point-cloud features through cross-attention mechanisms. Unlike these fusion paradigms, we directly exploit LiDAR in the 2D-to-3D view transformation process.

Height Modeling. Height is an important yet often overlooked attribute in BEV perception, providing geometric cues beyond planar layout. Motivated by the observation that objects are located at distinct height ranges, BEV-SAN [8] constructs a height histogram from LiDAR points to determine the boundaries of local BEV slices and then fuses these slices with global BEV features to improve detection accuracy. Beyond slice fusion, subsequent methods incorporate height cues directly into the view transformation process. OC-BEV [39] augments the uniform vertical sampling in BEVFormer [24] with a scene-level local height prior, thereby focusing sampling on height intervals where objects are most likely to appear. Extending this idea to finer granularity, HV-BEV [49] predicts a discrete height distribution for each BEV grid and selects the top-K values for feature sampling. Height cues are also important for 3D occupancy prediction, where vertical ambiguities can be more severe. For instance, DHD [50] decouples the projection space into multiple subspaces and employs the predicted height map to select features, alleviating height ambiguity. DA-Occ [58] instead leverages the height distribution to aggregate frustum features and further rearranges voxel features to apply direction-aware convolutions. Different from these explicit height-supervision paradigms, HBEVOcc [30] targets the loss of vertical information caused by folding the height dimension into BEV channels and proposes height-aware attention to implicitly capture latent vertical cues within BEV features. In contrast, we explicitly utilize a height map derived from LiDAR to reparameterize the projection space, enabling better alignment with the varying scene structure.

3 Method

3.1 Overview

As illustrated in Fig. 2, our framework consists of three stages. First, multi-view images are processed by the BEV Feature Extraction module, where a 2D encoder generates the depth distribution D and semantic features F_{sem} . These features are lifted into the BEV space through an LSS-based view transformation, yielding a coarse BEV feature F_{BEV} that serves as the initial BEV query. In parallel, the LiDAR point cloud is encoded by the LiDAR Height Encoding module into a BEV height map H_{lidar} , which is further conditioned by Progressive Height Conditioning during training to obtain the conditioned height map \hat{H} . Next, the Height-Guided Reparameterization module leverages \hat{H} to adaptively reparameterize each BEV pillar and mask out invalid BEV grids, refining the initial BEV query into \hat{Q} . Finally, \hat{Q} is fed into a 3D decoder for 3D occupancy prediction.

3.2 BEV Feature Extraction

Given multi-view input images, we first extract image features using a 2D encoder (e.g., ResNet [12]). For each camera view, the encoder predicts a depth distribution \mathbf{D} and a semantic feature map \mathbf{F}_{sem} from dense image features. The depth distribution represents the probability of each pixel belonging to predefined depth bins, while \mathbf{F}_{sem} captures appearance and contextual information for scene understanding. Following the LSS-based view transformation [21, 22, 37], we lift \mathbf{F}_{sem} from the 2D image plane into the BEV space using \mathbf{D} and the camera intrinsic and extrinsic parameters. This process yields a coarse BEV feature, denoted as \mathbf{F}_{BEV} , which serves as the initial BEV query for the subsequent Height-Guided Reparameterization module.

3.3 LiDAR Height Encoding

Height Map Generation. To efficiently encode sparse LiDAR observations, we project the input point cloud into a BEV height map. Given a point cloud $\mathcal{P} = \{(x_k, y_k, z_k)\}_{k=1}^K$ in the ego-vehicle coordinate system, we first define a 3D region of interest bounded within $[x_{\min}, x_{\max}]$, $[y_{\min}, y_{\max}]$, and $[z_{\min}, z_{\max}]$. The space is then discretized into a voxel grid with horizontal resolution Δ_{xy} and vertical resolution Δ_z . Each point $p_k \in \mathcal{P}$ is assigned to a voxel indexed by (i_x, i_y, i_z) :

$$(i_x, i_y, i_z) = \left(\left\lfloor \frac{x_k - x_{\min}}{\Delta_{xy}} \right\rfloor, \left\lfloor \frac{y_k - y_{\min}}{\Delta_{xy}} \right\rfloor, \left\lfloor \frac{z_k - z_{\min}}{\Delta_z} \right\rfloor \right). \quad (1)$$

Based on the voxelized point cloud, we construct a binary occupancy grid $\mathbf{V}_{\text{lidar}} \in \{0, 1\}^{X \times Y \times Z}$, where $\mathbf{V}_{\text{lidar}}(i_x, i_y, i_z) = 1$ if the corresponding voxel contains at least one LiDAR point. To obtain a 2D height representation, we collapse the 3D grid along the vertical axis by selecting the highest occupied voxel index of each non-empty BEV cell (i_x, i_y) :

$$i_z^*(i_x, i_y) = \max \{i_z \mid \mathbf{V}_{\text{lidar}}(i_x, i_y, i_z) = 1\}. \quad (2)$$

We then map the discrete index back to metric height $\mathbf{H}_{\text{lidar}} \in \mathbb{R}^{X \times Y}$ as:

$$\mathbf{H}_{\text{lidar}}(i_x, i_y) = z_{\min} + (i_z^*(i_x, i_y) + 1) \Delta_z, \quad (3)$$

where the upper boundary of the highest occupied voxel is taken as the representative height. For empty pillars satisfying $\sum_{i_z} \mathbf{V}_{\text{lidar}}(i_x, i_y, i_z) = 0$, we assign a default invalid value to $\mathbf{H}_{\text{lidar}}(i_x, i_y)$.

Progressive Height Conditioning. Directly using the LiDAR-derived height map $\mathbf{H}_{\text{lidar}}$ for Height-Guided Reparameterization may destabilize training, since $\mathbf{H}_{\text{lidar}}$ is inherently noisy, as evidenced by the error distribution in Fig. 2. As the height map directly determines the sampling locations of the subsequent module, such noise can lead to inaccurate sampling.

To mitigate this issue, we introduce a training-only Progressive Height Conditioning (PHC) strategy, which gradually shifts the conditioning signal from a dense ground-truth height map \mathbf{H}_{gt} to the noisy LiDAR height map $\mathbf{H}_{\text{lidar}}$. Here, \mathbf{H}_{gt} is derived from the occupancy ground truth using the same height extraction rule as in Eq. (2) and (3), ensuring that \mathbf{H}_{gt} and $\mathbf{H}_{\text{lidar}}$ are geometrically aligned. During training, the final conditioning map $\hat{\mathbf{H}}$ is generated by:

$$\hat{\mathbf{H}} = \psi(\mathbf{H}_{\text{lidar}}, \mathbf{H}_{\text{gt}}, \rho(e)), \quad (4)$$

where $\psi(\cdot)$ denotes a stochastic mixing function that independently replaces each valid BEV grid in $\mathbf{H}_{\text{lidar}}$ with the corresponding value from \mathbf{H}_{gt} with probability $\rho(e)$, while keeping the remaining grids unchanged. The mixing ratio $\rho(e)$ follows a cosine annealing schedule over E epochs:

$$\rho(e) = \frac{1}{2} \left(1 + \cos \left(\frac{\pi e}{E} \right) \right). \quad (5)$$

As a result, training starts with strong guidance from \mathbf{H}_{gt} when $\rho(e) = 1$, and gradually transitions to the LiDAR-based setting used at inference as $\rho(e)$ decreases to zero. During inference, PHC is disabled and the conditioning map is simply given by $\hat{\mathbf{H}} = \mathbf{H}_{\text{lidar}}$. In this way, PHC stabilizes early training and improves the robustness of height-guided sampling against noisy LiDAR observations.

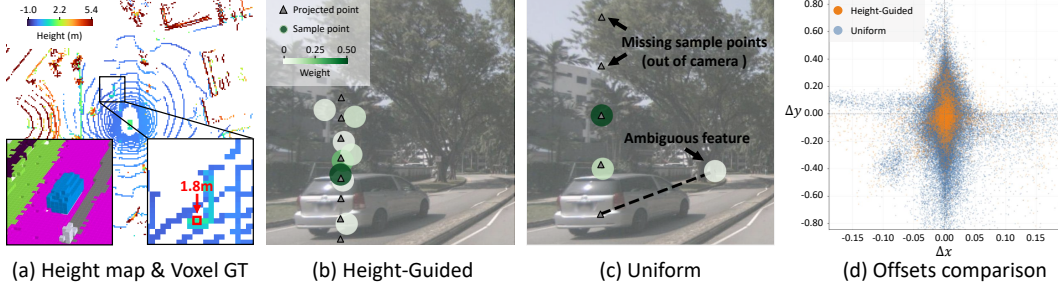


Figure 3: Comparison of height-guided and uniform sampling. (a) Height map and voxel ground truth of a vehicle. (b) Height-guided sampling concentrates projected reference points and sampled features around the valid object region. (c) Uniform sampling introduces invalid projections, including out-of-camera samples and ambiguous feature correspondences. (d) Learned cross-attention offsets show that Height-Guided Reparameterization yields a more compact distribution than uniform sampling.

3.4 Height-Guided Reparameterization

Revisiting Standard Backward Projection. In standard BEVFormer-style backward projection [23, 24, 26], each BEV query aggregates image features from a set of 3D reference points sampled uniformly along a globally fixed pillar:

$$\hat{Q}(i_x, i_y) = \sum_{j=1}^{N_z} \phi(Q(i_x, i_y), \mathcal{R}(i_x, i_y, z_j), \mathbf{F}_{\text{sem}}), \quad (6)$$

where $Q(i_x, i_y)$ and $\hat{Q}(i_x, i_y)$ denote the input and updated BEV queries at location (i_x, i_y) , $\phi(\cdot)$ represents the deformable cross-attention operator [24], $\mathcal{R}(i_x, i_y, z_j)$ stands for the 3D reference point at height z_j , \mathbf{F}_{sem} refers to the multi-view image features, and N_z is the number of vertical sampling points. The vertical sampling locations [23, 24, 26] are uniformly defined as:

$$z_j = z_{\min} + \alpha_j(z_{\max} - z_{\min}), \quad \alpha_j = \frac{j-1}{N_z-1}. \quad (7)$$

Since the vertical sampling locations $\{z_j\}_{j=1}^{N_z}$ are identical for all BEV grids, this formulation is inherently agnostic to scene geometry. As a result, reference points are often wasted in empty spaces, and even for object regions, the uniform sampling causes their 2D projections to misalign with the actual targets, leading to ambiguous correspondences and unreliable feature aggregation.

Reparameterization. To deal with this problem, we propose utilizing the conditioned height map $\hat{H}(i_x, i_y)$ to dynamically reparameterize the projection space of each BEV query.

Specifically, we define a height-validity mask:

$$M(i_x, i_y) = \mathbb{I}(\hat{H}(i_x, i_y) \text{ is valid}), \quad (8)$$

and construct height-guided sampling locations as:

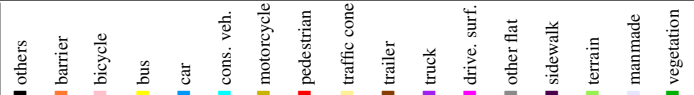
$$\tilde{z}_j(i_x, i_y) = z_{\min} + \alpha_j(\hat{H}(i_x, i_y) - z_{\min}), \quad \alpha_j = \frac{j-1}{N_z-1}. \quad (9)$$

Accordingly, the query update process is reformulated as:

$$\hat{Q}(i_x, i_y) = \begin{cases} \sum_{j=1}^{N_z} \phi(Q(i_x, i_y), \mathcal{R}(i_x, i_y, \tilde{z}_j(i_x, i_y)), \mathbf{F}_{\text{sem}}), & M(i_x, i_y) = 1, \\ Q(i_x, i_y), & M(i_x, i_y) = 0. \end{cases} \quad (10)$$

In this way, the conditioned height map \hat{H} defines the upper height bound of each pillar and restricts feature aggregation to valid BEV regions. The effectiveness of this reparameterization is illustrated in Fig. 3. Consider a target vehicle with a physical height of 1.8 m, as indicated by the LiDAR height map in Fig. 3(a). Under the standard uniform sampling paradigm (Fig. 3(c)), the model samples reference points up to the maximum predefined ceiling (e.g., $z_{\max} = 5.4$ m). This lack of geometric

Table 1: Performance on Occ3D. The camera visible mask is used during training. Inputs include Camera (C), Radar (R) and LIDAR (L). R denotes ResNet, and Swin denotes Swin Transformer.

Method	Input	Backbone	mIoU																		
				others	barrier	bicycle	bus	car	cons. veh.	motorcycle	pedestrian	traffic cone	trailer	truck	drive. surf.	other flat	sidewalk	terrain	manmade	vegetation	
BEVDetOcc [15]	C	Swin-B	42.0	12.2	49.6	25.1	52.0	54.5	27.9	28.0	28.9	27.2	36.4	42.2	82.3	43.3	54.6	57.9	48.6	43.6	
FB-Occ [23]	C	R50	39.8	13.8	44.5	27.1	46.2	49.7	24.6	27.4	28.5	28.2	33.7	36.5	81.7	44.1	52.6	56.9	42.6	38.1	
FlashOcc [54]	C	R50	32.0	6.2	39.6	11.3	36.3	44.0	16.3	14.7	16.9	15.8	28.6	30.9	78.2	37.5	47.4	51.4	36.8	31.4	
COTR [31]	C	R50	44.5	13.3	52.1	32.0	46.0	55.6	32.6	32.8	30.4	34.1	37.7	41.8	84.5	46.2	57.6	60.7	52.0	46.3	
ProtoOcc [19]	C	R50	39.6	12.4	45.9	26.3	44.4	51.8	26.8	27.6	28.0	27.5	32.8	36.9	81.8	45.7	53.1	56.5	42.2	36.6	
STCOcc [26]	C	R50	45.0	15.2	52.3	32.2	50.5	56.5	31.7	33.9	33.4	33.8	38.9	44.9	83.9	47.4	57.1	60.1	50.6	42.7	
RadOcc [55]	C+L	Swin-B	49.4	10.9	58.2	25.0	57.9	62.9	34.0	33.5	50.1	32.1	48.9	52.1	82.9	42.7	55.3	58.3	68.6	66.0	
OccFusion [33]	C+L+R	R101	46.7	12.4	50.3	31.5	57.6	58.8	34.0	41.0	47.2	29.7	42.0	48.0	78.4	35.7	47.3	52.7	63.5	63.3	
HyDRa [48]	C+R	R50	44.4	15.1	51.1	32.7	52.3	56.3	29.4	35.9	35.1	33.7	39.1	44.1	80.4	45.1	52.0	55.3	52.1	44.4	
EFFOcc [40]	C+L	R50	52.8	12.1	59.7	33.4	<u>61.8</u>	<u>65.0</u>	35.5	46.0	57.1	41.0	47.9	54.6	82.8	44.0	56.4	60.2	71.1	69.6	
SDG-Fusion [111]	C+L	R50	51.7	13.2	57.8	24.3	60.3	64.3	36.2	39.4	52.4	35.8	50.9	53.7	84.6	47.5	58.0	61.6	<u>70.7</u>	67.7	
SDG-KL [11]	C+L	R50	50.2	12.3	57.1	23.7	58.8	62.7	34.6	36.2	50.1	32.1	49.9	51.2	84.1	46.1	57.2	61.5	69.6	65.8	
ALOcc-2D-mini [3]	C+L	R50	50.0	15.7	54.6	36.6	55.7	60.6	34.8	41.0	44.9	39.3	44.5	51.1	83.6	48.5	57.3	60.2	62.7	58.2	
ALOcc-2D [3]	C+L	R50	53.5	<u>16.5</u>	<u>57.8</u>	41.6	57.9	63.8	37.6	45.0	52.1	<u>45.8</u>	49.6	54.4	85.3	<u>50.5</u>	<u>59.7</u>	<u>62.3</u>	67.1	62.0	
DAOcc [53]	C+L	R50	<u>54.3</u>	13.0	60.7	39.8	64.0	66.5	36.3	49.0	60.1	44.3	<u>50.7</u>	55.9	82.9	44.6	56.8	60.6	70.1	<u>68.3</u>	
HiPR-mini	C+L	R50	53.1	17.0	58.8	38.8	58.0	62.8	<u>37.7</u>	45.4	55.7	43.1	49.3	53.5	83.9	49.3	57.9	60.7	66.9	63.8	
HiPR	C+L	R50	54.7	16.4	<u>59.7</u>	<u>40.4</u>	59.7	64.9	38.9	<u>47.8</u>	<u>57.5</u>	46.2	48.9	<u>55.3</u>	<u>85.2</u>	51.6	59.9	62.7	69.1	65.4	

awareness results in numerous invalid projections that either fall out of the camera field of view or sample ambiguous background features (e.g., trees). In contrast, by dynamically truncating the sampling range to the actual object height ($[z_{\min}, 1.8]$ m), our height-guided method encourages the sampling points to concentrate on the semantically meaningful vehicle body (Fig. 3(b)). Furthermore, as shown in Fig. 3(d), the learned spatial offsets ($\Delta x, \Delta y$) of our method exhibit a compact, zero-centered distribution. This suggests that the initial 3D projections are well aligned with informative regions and require only minor adjustments. In contrast, uniform sampling produces a more scattered distribution, indicating that the model relies on larger offsets to capture valid features.

3.5 Loss Function

Following [3, 7, 27], we train the query-based decoder with a classification loss, a mask loss, and a dice loss. The overall objective is defined as:

$$\mathcal{L} = \lambda_{\text{cls}} \mathcal{L}_{\text{cls}} + \lambda_{\text{mask}} \mathcal{L}_{\text{mask}} + \lambda_{\text{dice}} \mathcal{L}_{\text{dice}}, \quad (11)$$

where \mathcal{L}_{cls} denotes the cross-entropy loss for query classification, $\mathcal{L}_{\text{mask}}$ denotes the cross-entropy loss for occupancy masks, and $\mathcal{L}_{\text{dice}}$ denotes the dice loss for mask overlap optimization. In our implementation, the loss weights are set to $\lambda_{\text{cls}} = 2.0$, $\lambda_{\text{mask}} = 5.0$, and $\lambda_{\text{dice}} = 5.0$.

4 Experiments

Datasets and Metrics. We evaluate our method on the nuScenes dataset [1], which contains 700 training scenes and 150 validation scenes with annotations at 2 Hz. Based upon nuScenes, Occ3D [42] and SurroundOcc [46] further provide voxel-wise occupancy annotations. For Occ3D, the voxel region spans $[-40, 40]$ m along the X and Y axes and $[-1, 5.4]$ m along the Z axis, with a voxel size of $0.4 \times 0.4 \times 0.4$ m. It contains 18 semantic categories, including 17 object classes and 1 empty class. For SurroundOcc, the voxel region is $[-50, 50]$ m along the X and Y axes and $[-5, 3]$ m along the Z axis, with a voxel size of $0.5 \times 0.5 \times 0.5$ m. Compared with Occ3D, SurroundOcc excludes the “others” category. Following prior work [26, 27, 53], we use mIoU and RayIoU as evaluation metrics.

Implementation Details. Built upon the ALOcc series [3], we develop two variants: a lightweight **HiPR-mini** for real-time performance, and a standard **HiPR** that incorporates stereo depth estimation and larger channel dimensions. We optimize all models using AdamW [29] with an initial learning rate of 2×10^{-4} for 24 epochs and a total batch size of 16. Our implementation is built on MMDetection3D [6]. Experiments are conducted on NVIDIA GeForce RTX 4090 and L40X GPUs.

Table 2: Comparison of RayIoU on Occ3D. The camera visible mask is not used during the training.

Method	Input	Backbone	RayIoU	RayIoU _{1m, 2m, 4m}
BEVFormer [24]	C	R101	32.4	26.1 32.9 38.0
FB-Occ [23]	C	R50	39.0	33.0 40.0 44.0
RenderOcc [36]	C	Swin-B	24.4	13.4 19.6 25.5
SparseOcc [27]	C	R50	36.1	30.2 36.8 41.2
FlashOcc [54]	C	R50	38.5	32.8 39.3 43.4
OPUS [44]	C	R50	41.2	34.7 42.1 46.7
STCOcc [26]	C	R50	42.1	36.9 42.8 46.7
ALOcc-2D-mini [3]	C	R50	39.3	32.9 40.1 44.8
ALOcc-2D [3]	C	R50	43.0	37.1 43.8 48.2
DAOcc [53]	C+L	R50	<u>48.4</u>	<u>44.5</u> 48.9 51.9
HiPR-mini	C+L	R50	<u>48.4</u>	<u>44.2</u> <u>49.0</u> <u>52.0</u>
HiPR	C+L	R50	50.0	45.9 50.5 53.4

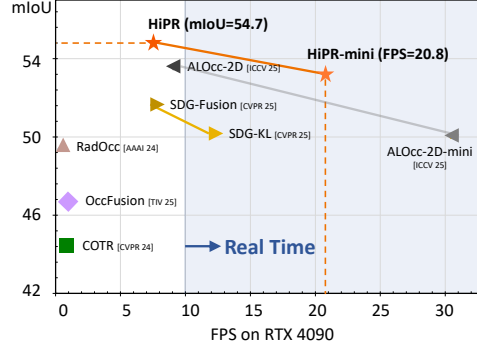


Figure 4: FPS-mIoU comparison.

Table 3: Performance on SurroundOcc. Unlike Occ3D, the evaluation is performed over all voxels.

Method	Input	Backbone	mIoU	Class															
				barrier	bicycle	bus	car	cons. veh.	motorcycle	pedestrian	traffic cone	trailer	truck	drive. surf.	other flat	sidewalk	terrain	manmade	vegetation
BEVFormer [24]	C	R101	16.8	14.2	6.6	23.5	28.3	8.7	10.8	6.6	4.1	11.2	17.8	37.3	18.0	22.9	22.2	13.8	22.2
TPVFormer [16]	C	R101	17.1	16.0	5.3	23.9	27.3	9.8	8.7	7.1	5.2	11.0	19.2	38.9	21.3	24.3	23.2	11.7	20.8
SurroundOcc [46]	C	R101	20.3	20.6	11.7	28.1	30.9	10.7	15.1	14.1	12.1	14.4	22.3	37.3	23.7	24.5	22.8	14.9	21.9
GaussianFormer [17]	C	R101	17.3	19.5	11.3	26.1	29.8	10.5	13.8	12.6	8.7	12.7	21.6	39.6	23.3	24.5	23.0	9.6	19.1
GaussianFormer2 [18]	C	R101	20.8	21.4	13.4	28.5	30.8	10.9	15.8	13.6	10.5	14.0	22.9	40.6	24.4	26.1	24.3	13.8	22.0
M-CONet [45]	C+L	R101	24.7	24.8	13.0	31.6	34.8	14.6	18.0	20.0	14.7	20.0	26.6	39.2	22.8	26.1	26.0	26.0	37.1
Co-Occ [35]	C+L	R101	27.1	28.1	16.1	34.0	<u>37.2</u>	17.0	21.6	20.8	15.9	21.9	28.7	42.3	25.4	<u>29.1</u>	<u>28.6</u>	28.2	38.0
OccFusion [33]	C+L	R101	27.6	25.2	19.9	34.8	36.2	20.0	23.1	25.3	17.5	22.7	30.1	39.5	23.3	25.7	27.6	29.5	40.6
OccFusion [33]	C+L+R	R101	28.3	<u>28.3</u>	21.0	35.1	36.8	20.3	26.2	25.9	19.2	21.3	<u>30.6</u>	40.1	23.8	25.6	27.6	29.8	40.8
OccCylindrical [34]	C+L	R50	<u>28.7</u>	26.2	<u>22.1</u>	31.5	36.8	18.0	<u>27.8</u>	29.9	23.9	20.6	28.3	<u>43.0</u>	23.1	28.0	27.8	30.8	41.0
HiPR-mini	C+L	R50	28.6	27.9	21.7	33.2	36.8	<u>22.8</u>	27.7	27.0	19.9	20.2	30.0	41.4	<u>26.8</u>	28.7	27.7	28.3	37.5
HiPR	C+L	R50	30.4	29.9	23.1	<u>34.8</u>	38.4	23.4	29.7	<u>28.8</u>	<u>21.9</u>	<u>22.4</u>	32.0	43.8	28.6	30.6	29.9	<u>30.6</u>	39.4

4.1 Comparison with the State-of-the-Art

Comparison on Occ3D. As shown in Tab. 1 and Tab. 2, we evaluate HiPR on Occ3D under both training settings: with and without the camera mask. Overall, our method achieves state-of-the-art performance in both scenarios. Under the *with camera mask* setting, we report mIoU. HiPR outperforms the second-best DAOcc [53] by 0.4 mIoU. Compared to OccFusion [33], which leverages additional radar input and a larger backbone (ResNet-101 [12]), HiPR achieves a substantial gain of 8.0 mIoU. Under the *without camera mask* setting, we report RayIoU [27]. HiPR significantly outperforms camera-based methods such as STCOcc [26] by a large margin of 7.9 RayIoU. Compared to the multi-modal method DAOcc, the lightweight variant HiPR-mini achieves comparable performance, while the full HiPR further improves upon it by 1.6 RayIoU. Fig. 5 shows qualitative comparisons between HiPR and DAOcc. DAOcc misclassifies large objects and fails to reconstruct distant structures accurately, while HiPR yields more accurate semantics and more complete reconstructions.

Comparison on SurroundOcc. Tab. 3 presents a quantitative comparison on the SurroundOcc [46] dataset. Overall, HiPR consistently outperforms existing methods. In particular, it surpasses the second-best method, OccCylindrical [34], by 1.7 mIoU. Meanwhile, despite using only a lightweight ResNet-50 [12] backbone, HiPR still outperforms competitive approaches such as OccFusion [33], Co-Occ [35], and GaussianFormer [17]. Furthermore, HiPR achieves clear improvements on challenging categories such as bicycle and motorcycle, which are typically sparse and difficult to model, thereby demonstrating its ability to better capture fine-grained structures.

Speed–Accuracy Trade-off. Fig. 4 presents the speed–accuracy trade-off of HiPR on Occ3D under the setting trained without camera visible mask. Following prior works [13, 14, 19], methods running above 10 FPS are regarded as real-time. Overall, HiPR attains state-of-the-art accuracy, while HiPR-mini enables real-time inference with near state-of-the-art performance, outperforming existing feature-fusion-based multi-modal methods [11, 33, 55]. Specifically, compared with the real-time method SDG-KL [11], HiPR-mini is 7.2 FPS faster and improves mIoU by 2.9 points, demonstrating its superior speed–accuracy trade-off for efficient 3D occupancy prediction.

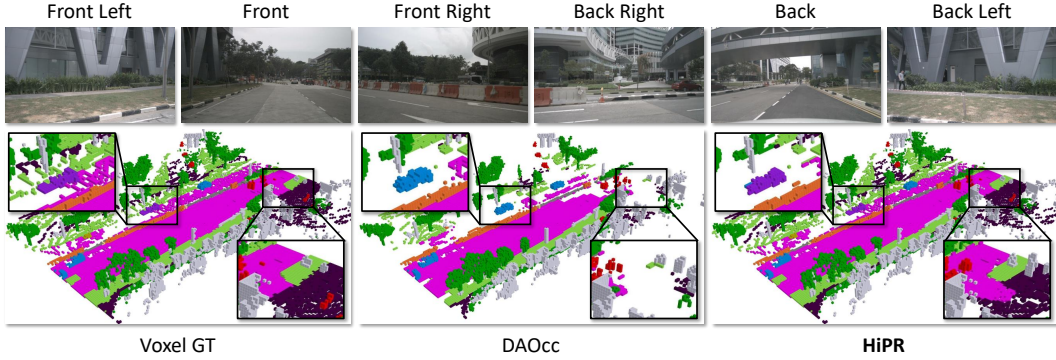


Figure 5: Visual comparisons of DAOcc and our HiPR on the validation set of Occ3D.

Table 4: Ablation study of HiPR on the Occ3D dataset. HGR refers to the Height-Guided Reparameterization and PHC refers to the Progressive Height Conditioning.

Model	HGR		PHC	mIoU
	Height-Guided Sampling	Height-Validity Mask		
Baseline				50.01
i	✓			51.04
ii	✓		✓	52.81
iii	✓	✓	✓	53.10

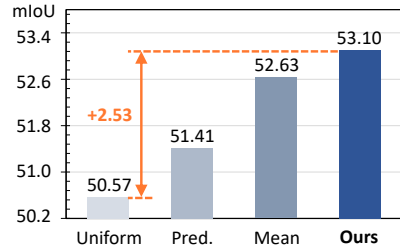


Figure 6: Ablation on HGR.

4.2 Ablation Study

All experiments in this section are trained with the camera visible mask on the Occ3D dataset.

HiPR Designs. Tab. 4 presents the ablation study of the proposed Height-Guided Reparameterization (HGR) and Progressive Height Conditioning (PHC). The baseline model is ALOcc-2D-mini [3]. Starting from this baseline, introducing height-guided sampling improves the mIoU from 50.01 to 51.04. In this setting, valid pillars are reparameterized according to the height map, while invalid regions still use uniformly sampled pillars over the maximum height range. Further incorporating the height-validity mask brings a larger improvement, boosting the mIoU to 52.81. This demonstrates that restricting feature aggregation to valid BEV regions is crucial for suppressing invalid projections and improving geometric alignment. As shown in Fig. 7, the resulting BEV features are more focused and semantically consistent in occupied regions, while noisy responses in empty areas are effectively suppressed. Finally, PHC further improves the performance by 0.29 mIoU, indicating that progressively transitioning stabilizes training and improves the robustness of height-guided sampling.

Sampling Strategies in HGR. Fig. 6 compares different height sampling strategies in HGR. Starting from HiPR-mini, we keep all other components fixed and only replace the height-guided sampling strategy. Using a uniform sampling range from z_{\min} to z_{\max} achieves 50.57 mIoU. Replacing it with a learned height predictor improves performance to 51.41 mIoU, demonstrating the benefit of adaptive height modeling. Specifically, in this setting, we remove the LiDAR branch and append a height prediction head to the BEV features, supervised by a cross-entropy loss. The improvement over uniform sampling indicates that fixed sampling is suboptimal for scenes with varying local geometry, while adaptive height estimation provides a more suitable sampling prior. Introducing LiDAR geometry further improves performance. Using the mean pillar height reaches 52.63 mIoU, while our strategy of using the highest LiDAR-observed height achieves the best result of 53.10 mIoU. These results show that LiDAR-guided height sampling is more effective than learned or uniform alternatives, and that the highest occupied height provides the most informative prior for HGR.

Conditioning Strategy in PHC. As shown in Tab. 5, we compare different conditioning strategies in PHC. Using only LiDAR-derived heights as the baseline achieves 52.81 mIoU. In contrast, using ground-truth heights throughout training severely degrades performance to 31.83 mIoU, revealing a large gap between the clean training signal and noisy LiDAR at inference. We further compare two mixing strategies. Linear interpolation blends ground-truth and LiDAR-derived height maps but brings only limited improvement, while our hard replacement strategy achieves the best performance

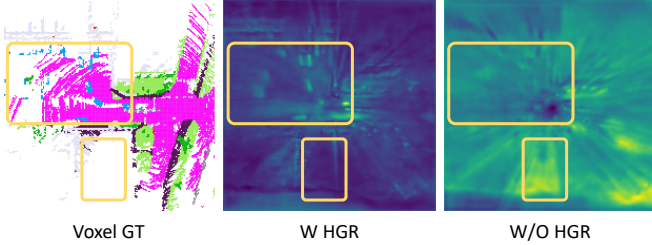


Figure 7: Comparison of BEV feature with and without HGR.

Table 5: Ablation study of conditioning strategy in PHC module.

Setting	mIoU
LiDAR Only	52.81
GT Only	31.83
Linear Interpolation	52.83
Replace (Ours)	53.10

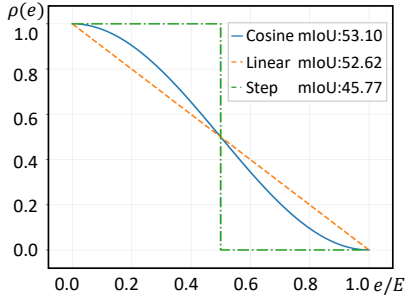


Figure 8: PHC schedules ablation.

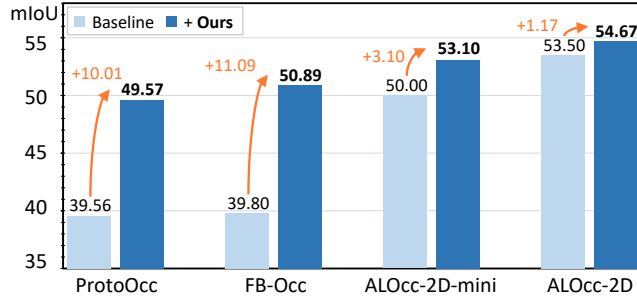


Figure 9: Generalization on different architectures.

of 53.10 mIoU. Moreover, we ablate different PHC schedules in Fig. 8. The step schedule causes an abrupt transition and degrades performance by 7.33 mIoU, whereas the cosine schedule gradually shifts from ground-truth to LiDAR-derived heights and achieves the best result.

4.3 Generalization Capability

We further incorporate our design into different occupancy frameworks to evaluate its generalization capability, including ProtoOcc [19], FB-Occ [23], and the ALOcc-2D series [3]. For ProtoOcc and ALOcc, we insert the proposed HGR before the occupancy head, while for FB-Occ, we directly replace the standard backward projection with HGR. All models are trained with PHC. As shown in Fig. 9, our method consistently improves the baseline models across different architectures. Specifically, applying our method to the camera-based ProtoOcc and FB-Occ brings substantial gains of 10.01 and 11.09 mIoU, respectively. When applied to ALOcc variants that utilize LiDAR depth ground truth for feature lifting, our method still achieves improvements of 3.10 and 1.17 mIoU. These consistent gains demonstrate that the proposed HGR and PHC are not tied to a specific framework, but can serve as general and effective plug-and-play modules for 3D occupancy prediction pipelines.

5 Conclusion

In this paper, we present HiPR, a novel camera–LiDAR framework that reparameterizes the projection space using the LiDAR height prior. By encoding LiDAR observations into a BEV height map, HiPR introduces height-guided sampling and height-validity mask to adaptively adjust sampling range and grid validity, thereby improving geometric alignment in the projection space. In addition, we leverage ground-truth heights during training to stabilize optimization. Extensive experiments demonstrate the superiority of HiPR in accuracy, efficiency, and generalization.

Limitation. Although HiPR achieves strong performance, it relies on LiDAR-derived height prior, which can become sparse and less reliable in distant regions. In addition, modeling scene geometry with a single height representation may be insufficient for complex multi-layer structures. We leave the exploration of richer geometric representations and more robust height prior as future work.

Broader Impact. With the rapid development of multi-modal autonomous driving systems, improving the accuracy and efficiency of 3D scene understanding has become increasingly important. HiPR represents a step forward in this direction by enhancing geometric alignment in occupancy prediction while maintaining real-time performance. Given the broad relevance of 3D scene understanding, our approach has the potential to benefit a wide range of autonomous driving applications.

References

- [1] Holger Caesar, Varun Bankiti, Alex H Lang, Sourabh Vora, Venice Erin Liong, Qiang Xu, Anush Krishnan, Yu Pan, Giancarlo Baldan, and Oscar Beijbom. nuscenes: A multimodal dataset for autonomous driving. In *Proceedings of the IEEE/CVF conference on computer vision and pattern recognition*, pages 11621–11631, 2020.
- [2] Anh-Quan Cao and Tuan-Hung Vu. Occany: Generalized unconstrained urban 3d occupancy. In *Conference on Computer Vision and Pattern Recognition (CVPR)*, 2026.
- [3] Dubing Chen, Jin Fang, Wencheng Han, Xinjing Cheng, Junbo Yin, Chengzhong Xu, Fahad Shahbaz Khan, and Jianbing Shen. Alocc: Adaptive lifting-based 3d semantic occupancy and cost volume-based flow predictions. In *Proceedings of the IEEE/CVF International Conference on Computer Vision*, pages 4156–4166, 2025.
- [4] Dubing Chen, Huan Zheng, Jin Fang, Xingping Dong, Xianfei Li, Wenlong Liao, Tao He, Pai Peng, and Jianbing Shen. Rethinking temporal fusion with a unified gradient descent view for 3d semantic occupancy prediction. In *Proceedings of the IEEE/CVF Conference on Computer Vision and Pattern Recognition*, pages 1505–1515, 2025.
- [5] Dubing Chen, Huan Zheng, Yucheng Zhou, Xianfei Li, Wenlong Liao, Tao He, Pai Peng, and Jianbing Shen. Semantic causality-aware vision-based 3d occupancy prediction. In *Proceedings of the IEEE/CVF International Conference on Computer Vision*, pages 24878–24888, 2025.
- [6] Kai Chen, Jiaqi Wang, Jiangmiao Pang, Yuhang Cao, Yu Xiong, Xiaoxiao Li, Shuyang Sun, Wansen Feng, Ziwei Liu, Jiarui Xu, et al. Mmdetection: Open mmlab detection toolbox and benchmark. *arXiv preprint arXiv:1906.07155*, 2019.
- [7] Bowen Cheng, Ishan Misra, Alexander G Schwing, Alexander Kirillov, and Rohit Girdhar. Masked-attention mask transformer for universal image segmentation. In *Proceedings of the IEEE/CVF conference on computer vision and pattern recognition*, pages 1290–1299, 2022.
- [8] Xiaowei Chi, Jiaming Liu, Ming Lu, Rongyu Zhang, Zhaoqing Wang, Yandong Guo, and Shanghang Zhang. Bev-san: Accurate bev 3d object detection via slice attention networks. In *Proceedings of the IEEE/CVF Conference on Computer Vision and Pattern Recognition*, pages 17461–17470, 2023.
- [9] Chenxu Dang, Haiyan Liu, Jason Bao, Pei An, Xinyue Tang, An Pan, Jie Ma, Bingchuan Sun, and Yan Wang. Sparseworld: A flexible, adaptive, and efficient 4d occupancy world model powered by sparse and dynamic queries. In *Proceedings of the AAAI Conference on Artificial Intelligence*, pages 3497–3505, 2026.
- [10] Jiayuan Du, Yiming Zhao, Zhenglong Guo, Yong Pan, Wenbo Hou, Zhihui Hao, Kun Zhan, and Qijun Chen. Sparseworld-tc: Trajectory-conditioned sparse occupancy world model. *arXiv preprint arXiv:2511.22039*, 2025.
- [11] ZaiPeng Duan, ChenXu Dang, Xuzhong Hu, Pei An, Junfeng Ding, Jie Zhan, YunBiao Xu, and Jie Ma. Sdgocc: Semantic and depth-guided bird’s-eye view transformation for 3d multi-modal occupancy prediction. In *Proceedings of the Computer Vision and Pattern Recognition Conference*, pages 6751–6760, 2025.
- [12] Kaiming He, Xiangyu Zhang, Shaoqing Ren, and Jian Sun. Deep residual learning for image recognition. In *Proceedings of the IEEE conference on computer vision and pattern recognition*, pages 770–778, 2016.
- [13] Yulin He, Wei Chen, Siqi Wang, Tianci Xun, and Yusong Tan. Achieving speed-accuracy balance in vision-based 3d occupancy prediction via geometric-semantic disentanglement. In *Proceedings of the AAAI Conference on Artificial Intelligence*, pages 3455–3463, 2025.
- [14] Jiawei Hou, Xiaoyan Li, Wenhao Guan, Gang Zhang, Di Feng, Yuheng Du, Xiangyang Xue, and Jian Pu. Fastocc: Accelerating 3d occupancy prediction by fusing the 2d bird’s-eye view and perspective view. In *2024 IEEE International Conference on Robotics and Automation (ICRA)*, pages 16425–16431. IEEE, 2024.

- [15] Junjie Huang, Guan Huang, Zheng Zhu, Yun Ye, and Dalong Du. Bevdet: High-performance multi-camera 3d object detection in bird-eye-view. *arXiv preprint arXiv:2112.11790*, 2021.
- [16] Yuanhui Huang, Wenzhao Zheng, Yunpeng Zhang, Jie Zhou, and Jiwen Lu. Tri-perspective view for vision-based 3d semantic occupancy prediction. In *Proceedings of the IEEE/CVF conference on computer vision and pattern recognition*, pages 9223–9232, 2023.
- [17] Yuanhui Huang, Wenzhao Zheng, Yunpeng Zhang, Jie Zhou, and Jiwen Lu. Gaussianformer: Scene as gaussians for vision-based 3d semantic occupancy prediction. In *European Conference on Computer Vision*, pages 376–393. Springer, 2024.
- [18] Yuanhui Huang, Amonnut Thammatadatrakoon, Wenzhao Zheng, Yunpeng Zhang, Dalong Du, and Jiwen Lu. Gaussianformer-2: Probabilistic gaussian superposition for efficient 3d occupancy prediction. In *Proceedings of the computer vision and pattern recognition conference*, pages 27477–27486, 2025.
- [19] Jungho Kim, Changwon Kang, Dongyoung Lee, Sehwan Choi, and Jun Won Choi. Protoocc: Accurate, efficient 3d occupancy prediction using dual branch encoder-prototype query decoder. In *Proceedings of the AAAI Conference on Artificial Intelligence*, pages 4284–4292, 2025.
- [20] Ziyang Leng, Jiawei Yang, Wenlong Yi, and Bolei Zhou. Occupancy learning with spatiotemporal memory. In *Proceedings of the IEEE/CVF International Conference on Computer Vision*, pages 26569–26578, 2025.
- [21] Yin hao Li, Han Bao, Zheng Ge, Jinrong Yang, Jianjian Sun, and Zeming Li. Bevstereo: Enhancing depth estimation in multi-view 3d object detection with temporal stereo. In *Proceedings of the AAAI conference on artificial intelligence*, pages 1486–1494, 2023.
- [22] Yin hao Li, Zheng Ge, Guanyi Yu, Jinrong Yang, Zengran Wang, Yukang Shi, Jianjian Sun, and Zeming Li. Bevdepth: Acquisition of reliable depth for multi-view 3d object detection. In *Proceedings of the AAAI conference on artificial intelligence*, pages 1477–1485, 2023.
- [23] Zhiqi Li, Zhiding Yu, David Austin, Mingsheng Fang, Shiyi Lan, Jan Kautz, and Jose M Alvarez. Fb-occ: 3d occupancy prediction based on forward-backward view transformation. *arXiv preprint arXiv:2307.01492*, 2023.
- [24] Zhiqi Li, Wenhai Wang, Hongyang Li, Enze Xie, Chonghao Sima, Tong Lu, Qiao Yu, and Jifeng Dai. Bevformer: learning bird’s-eye-view representation from lidar-camera via spatiotemporal transformers. *IEEE Transactions on Pattern Analysis and Machine Intelligence*, 47(3):2020–2036, 2024.
- [25] Zhihao Li, Shanshan Zhang, and Jian Yang. Ashsr: Enhancing query-based occupancy prediction via anti-occlusion sampling and hard sample reweighting. *Neurocomputing*, 676:133007, 2026.
- [26] Zhimin Liao, Ping Wei, Shuaijia Chen, Haoxuan Wang, and Ziyang Ren. Stcocc: Sparse spatial-temporal cascade renovation for 3d occupancy and scene flow prediction. In *Proceedings of the Computer Vision and Pattern Recognition Conference*, pages 1516–1526, 2025.
- [27] Haisong Liu, Yang Chen, Haiguang Wang, Zetong Yang, Tianyu Li, Jia Zeng, Li Chen, Hongyang Li, and Limin Wang. Fully sparse 3d occupancy prediction. In *European Conference on Computer Vision*, pages 54–71. Springer, 2024.
- [28] Ruixun Liu, Lingyu Kong, Derun Li, and Hang Zhao. Occvla: Vision-language-action model with implicit 3d occupancy supervision. *arXiv preprint arXiv:2509.05578*, 2025.
- [29] Ilya Loshchilov and Frank Hutter. Decoupled weight decay regularization. *arXiv preprint arXiv:1711.05101*, 2017.
- [30] Chuandong Lyu, Wenkai Li, Iman Yi Liao, Fengqian Ding, Han Liu, and Hongchao Zhou. Hbevocc: Height-aware bird’s-eye-view representation for 3d occupancy prediction from multi-camera images. *Sensors (Basel, Switzerland)*, 26(3):934, 2026.

- [31] Qihang Ma, Xin Tan, Yanyun Qu, Lizhuang Ma, Zhizhong Zhang, and Yuan Xie. Cotr: Compact occupancy transformer for vision-based 3d occupancy prediction. In *Proceedings of the IEEE/CVF Conference on Computer Vision and Pattern Recognition*, pages 19936–19945, 2024.
- [32] Yukai Ma, Jianbiao Mei, Xuemeng Yang, Licheng Wen, Weihua Xu, Jiangning Zhang, Xingxing Zuo, Botian Shi, and Yong Liu. Licrocc: Teach radar for accurate semantic occupancy prediction using lidar and camera. *IEEE Robotics and Automation Letters*, 10(1):852–859, 2024.
- [33] Zhenxing Ming, Julie Stephany Berrio, Mao Shan, and Stewart Worrall. Occfusion: Multi-sensor fusion framework for 3d semantic occupancy prediction. *IEEE Transactions on Intelligent Vehicles*, 2024.
- [34] Zhenxing Ming, Julie Stephany Berrio, Mao Shan, Yaoqi Huang, Hongyu Lyu, Nguyen Hoang Khoi Tran, Tzu-Yun Tseng, and Stewart Worrall. Occcylindrical: Multi-modal fusion with cylindrical representation for 3d semantic occupancy prediction. *arXiv preprint arXiv:2505.03284*, 2025.
- [35] Jingyi Pan, Zipeng Wang, and Lin Wang. Co-occ: Coupling explicit feature fusion with volume rendering regularization for multi-modal 3d semantic occupancy prediction. *IEEE Robotics and Automation Letters*, 9(6):5687–5694, 2024.
- [36] Mingjie Pan, Jiaming Liu, Renrui Zhang, Peixiang Huang, Xiaoqi Li, Hongwei Xie, Bing Wang, Li Liu, and Shanghang Zhang. Renderocc: Vision-centric 3d occupancy prediction with 2d rendering supervision. In *2024 IEEE International Conference on Robotics and Automation (ICRA)*, pages 12404–12411. IEEE, 2024.
- [37] Jonah Philion and Sanja Fidler. Lift, splat, shoot: Encoding images from arbitrary camera rigs by implicitly unprojecting to 3d. In *European conference on computer vision*, pages 194–210. Springer, 2020.
- [38] Irfan Qaisar, Kailai Sun, Dianyu Zhong, Xu Yang, Xi Miao, and Qianchuan Zhao. Occmamba: A mamba-based deep learning approach for indoor occupancy prediction. *Building and Environment*, page 114085, 2025.
- [39] Zhangyang Qi, Jiaqi Wang, Xiaoyang Wu, and Hengshuang Zhao. Ocbev: Object-centric bev transformer for multi-view 3d object detection. In *2024 International Conference on 3D Vision (3DV)*, pages 1188–1197. IEEE, 2024.
- [40] Yining Shi, Kun Jiang, Jinyu Miao, Ke Wang, Kangan Qian, Yunlong Wang, Jiushi Li, Tuopu Wen, Mengmeng Yang, Yiliang Xu, et al. Effocc: Learning efficient occupancy networks from minimal labels for autonomous driving. In *2025 IEEE/RSJ International Conference on Intelligent Robots and Systems (IROS)*, pages 17008–17015. IEEE, 2025.
- [41] Chaehee Song, Sanmin Kim, Hyeonjun Jeong, Juyeb Shin, Joonhee Lim, and Dongsuk Kum. Reocc: Camera-radar fusion with radar feature enrichment for 3d occupancy prediction. In *2025 IEEE/RSJ International Conference on Intelligent Robots and Systems (IROS)*, pages 15367–15374. IEEE, 2025.
- [42] Xiaoyu Tian, Tao Jiang, Longfei Yun, Yue Wang, Yilun Wang, and Hang Zhao. Occ3d: A large-scale 3d occupancy prediction benchmark for autonomous driving. *arXiv preprint arXiv:2304.14365*, 2023.
- [43] Guoqing Wang, Zhongdao Wang, Pin Tang, Jilai Zheng, Xiangxuan Ren, Bailan Feng, and Chao Ma. Occgen: Generative multi-modal 3d occupancy prediction for autonomous driving. In *European Conference on Computer Vision*, pages 95–112. Springer, 2024.
- [44] Jiabao Wang, Zhaojiang Liu, Qiang Meng, Liujiang Yan, Ke Wang, Jie Yang, Wei Liu, Qibin Hou, and Ming-Ming Cheng. Opus: occupancy prediction using a sparse set. *Advances in Neural Information Processing Systems*, 37:119861–119885, 2024.

- [45] Xiaofeng Wang, Zheng Zhu, Wenbo Xu, Yunpeng Zhang, Yi Wei, Xu Chi, Yun Ye, Dalong Du, Jiwen Lu, and Xingang Wang. Openoccupancy: A large scale benchmark for surrounding semantic occupancy perception. In *Proceedings of the IEEE/CVF International Conference on Computer Vision*, pages 17850–17859, 2023.
- [46] Yi Wei, Linqing Zhao, Wenzhao Zheng, Zheng Zhu, Jie Zhou, and Jiwen Lu. Surroundocc: Multi-camera 3d occupancy prediction for autonomous driving. In *Proceedings of the IEEE/CVF International Conference on Computer Vision*, pages 21729–21740, 2023.
- [47] Zhiqiang Wei, Lianqing Zheng, Jianan Liu, Tao Huang, Qing-Long Han, Wenwen Zhang, and Fengdeng Zhang. Ms-occ: Multi-stage lidar-camera fusion for 3d semantic occupancy prediction. *arXiv preprint arXiv:2504.15888*, 2025.
- [48] Philipp Wolters, Johannes Gilg, Torben Teepe, Fabian Herzog, Anouar Laouichi, Martin Hofmann, and Gerhard Rigoll. Unleashing hydra: Hybrid fusion, depth consistency and radar for unified 3d perception. In *2025 IEEE International Conference on Robotics and Automation (ICRA)*, pages 7467–7474. IEEE, 2025.
- [49] Di Wu, Feng Yang, Benlian Xu, Pan Liao, Wenhui Zhao, and Dingwen Zhang. Hv-bev: Decoupling horizontal and vertical feature sampling for multi-view 3d object detection. *IEEE Transactions on Intelligent Transportation Systems*, 2025.
- [50] Yuan Wu, Zhiqiang Yan, Zhengxue Wang, Xiang Li, Le Hui, and Jian Yang. Deep height decoupling for precise vision-based 3d occupancy prediction. In *2025 IEEE International Conference on Robotics and Automation (ICRA)*, pages 12647–12654. IEEE, 2025.
- [51] Yuan Wu, Zhiqiang Yan, Yigong Zhang, Xiang Li, and Jian Yang. See through the dark: Learning illumination-affined representations for nighttime occupancy prediction. *arXiv preprint arXiv:2505.20641*, 2025.
- [52] Yu Yang, Jianbiao Mei, Yukai Ma, Siliang Du, Wenqing Chen, Yijie Qian, Yuxiang Feng, and Yong Liu. Driving in the occupancy world: Vision-centric 4d occupancy forecasting and planning via world models for autonomous driving. In *Proceedings of the AAAI Conference on Artificial Intelligence*, pages 9327–9335, 2025.
- [53] Zhen Yang, Yanpeng Dong, Jiayu Wang, Heng Wang, Lichao Ma, Zijian Cui, Qi Liu, Haoran Pei, Kexin Zhang, and Chao Zhang. Daocc: 3d object detection assisted multi-sensor fusion for 3d occupancy prediction. *IEEE Transactions on Circuits and Systems for Video Technology*, 2025.
- [54] Zichen Yu, Changyong Shu, Jiajun Deng, Kangjie Lu, Zongdai Liu, Jiangyong Yu, Dawei Yang, Hui Li, and Yan Chen. Flashocc: Fast and memory-efficient occupancy prediction via channel-to-height plugin. *arXiv preprint arXiv:2311.12058*, 2023.
- [55] Haiming Zhang, Xu Yan, Dongfeng Bai, Jiantao Gao, Pan Wang, Bingbing Liu, Shuguang Cui, and Zhen Li. Radocc: Learning cross-modality occupancy knowledge through rendering assisted distillation. In *Proceedings of the AAAI Conference on Artificial Intelligence*, pages 7060–7068, 2024.
- [56] Lianqing Zheng, Jianan Liu, Runwei Guan, Long Yang, Shouyi Lu, Yuanzhe Li, Xiaokai Bai, Jie Bai, Zhixiong Ma, Hui-Liang Shen, et al. Doracamom: Joint 3d detection and occupancy prediction with multi-view 4d radars and cameras for omnidirectional perception. *IEEE Transactions on Circuits and Systems for Video Technology*, 2026.
- [57] Wenzhao Zheng, Weiliang Chen, Yuanhui Huang, Borui Zhang, Yueqi Duan, and Jiwen Lu. Occworld: Learning a 3d occupancy world model for autonomous driving. In *European conference on computer vision*, pages 55–72. Springer, 2024.
- [58] Yuchen Zhou, Yan Luo, Xiaogang Wang, Xingjian Gu, Mingzhou Lu, and Xiangbo Shu. Da-occ: Direction-aware 2d convolution for efficient and geometry-preserving 3d occupancy prediction in autonomous driving. *arXiv preprint arXiv:2507.23599*, 2025.
- [59] Xubo Zhu, Haoyang Zhang, Fei He, Rui Wu, Yanhu Shan, Wen Yang, and Huai Yu. Dr. occ: Depth-and region-guided 3d occupancy from surround-view cameras for autonomous driving. *arXiv preprint arXiv:2603.01007*, 2026.

A Technical appendices and supplementary material

Table 6: Comparison of computational cost. Metrics were measured on an NVIDIA 4090 GPU.

Method	mIoU	FPS	Parameters (M)	Training Memory (GB)	GPU Hours
FB-Occ [23]	39.80	14.4	68.53	6.01	210
+Ours	50.89	14.8	68.53	5.97	212
ALOcc-2D-mini [3]	50.00	30.5	36.23	2.15	62
+Ours	53.10	20.8	37.21	2.58	68
ALOcc-2D [3]	53.50	8.1	63.70	3.38	122
+Ours	54.67	7.5	63.96	4.58	134

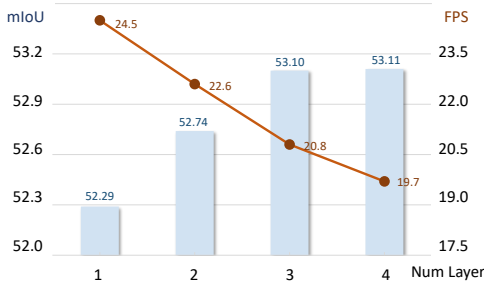


Figure 10: Ablation on HGP layers.

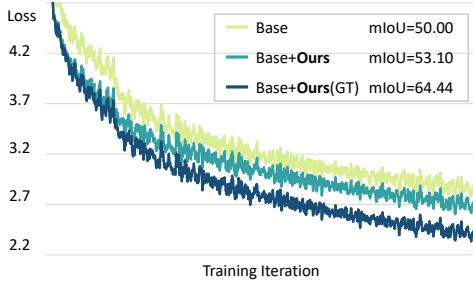


Figure 11: Upper-Bound analysis.

A.1 Ablation on HGP Layers

We conduct this ablation by varying the number of HGP layers in HiPR-mini. As shown in Fig. 10, mIoU performance consistently improves as the number of layers increases, but the gain becomes marginal beyond three layers, while FPS continues to decrease with additional computation. Therefore, we adopt three HGP layers to achieve a better accuracy-efficiency trade-off.

A.2 Computational Cost

Tab. 6 presents the computational cost analysis of our method on different models. Overall, our method consistently improves prediction accuracy with only limited additional computational overhead. Specifically, on FB-Occ [23], our method achieves a 27.9% improvement in mIoU. Meanwhile, by filtering out BEV grids with the height validity mask, our method reduces unnecessary computation and maintains comparable efficiency. For the LiDAR-depth-assisted ALOcc series [3], our method also brings consistent performance gains. On ALOcc-2D-mini, the mIoU increases from 50.00 to 53.10, with only a moderate increase in parameters and training memory. On ALOcc-2D, our method further improves the mIoU from 53.50 to 54.67, while maintaining comparable inference speed. These results demonstrate that our method can effectively enhance occupancy prediction accuracy across different baseline models without introducing prohibitive computational costs.

A.3 Upper-Bound Analysis

To evaluate the potential of height guidance, we compare the baseline ALOcc-2D-mini [3], our LiDAR-based height-guided variant, and an upper-bound model that leverages ground-truth height maps. Notably, the upper-bound setting uses ground-truth height not only during training but also at inference time. As illustrated in Fig. 11, incorporating LiDAR height guidance improves the baseline by 3.10 mIoU, demonstrating the effectiveness of our reparameterization strategy. Furthermore, ground-truth heights guidance accelerates convergence and yields substantially better performance, improving mIoU by 14.44. These results suggest that a more accurate height prior provide stronger geometric constraints and highlight the upper-bound potential of our height-guided design.

A.4 Additional Visual Results

As shown in Fig. 12, we provide additional visualizations of DAOcc [53] and our HiPR on Occ3D.

